

RESOLVING GAS DYNAMICS IN THE CIRCUMNUCLEAR REGION OF A DISK GALAXY IN A COSMOLOGICAL SIMULATION

ROBYN LEVINE^{1,2,3}, NICKOLAY Y. GNEDIN^{3,4,5}, ANDREW J. S. HAMILTON^{1,2}, AND ANDREY V. KRAVTSOV^{4,5,6}

Draft version February 2, 2008

ABSTRACT

Using a hydrodynamic adaptive mesh refinement code, we simulate the growth and evolution of a galaxy, which could potentially host a supermassive black hole, within a cosmological volume. Reaching a dynamical range in excess of 10 million, the simulation follows the evolution of the gas structure from super-galactic scales all the way down to the outer edge of the accretion disk. Here, we focus on global instabilities in the self-gravitating, cold, turbulence-supported, molecular gas disk at the center of the model galaxy, which provide a natural mechanism for angular momentum transport down to sub-pc scales. The gas density profile follows a power-law $\propto r^{-8/3}$, consistent with an analytic description of turbulence in a quasi-stationary circumnuclear disk. We analyze the properties of the disk which contribute to the instabilities, and investigate the significance of instability for the galaxy's evolution and the growth of a supermassive black hole at the center.

Subject headings: galaxies: evolution—galaxies: high-redshift—galaxies: ISM—galaxies: nuclei—galaxies: structure

1. INTRODUCTION AND MOTIVATION

It is increasingly evident that the growth histories of different components of galaxies: stars, gas, and supermassive black holes, are intricately connected. Observations indicate a relationship between the masses of supermassive black holes (SMBHs) and various properties of their host galaxies, such as the spheroid mass (Magorrian et al. 1998) and the velocity dispersion of stars in the bulge (Ferrarese & Merritt 2000; Gebhardt et al. 2000; Tremaine et al. 2002). Recent simulations have shown that feedback from accreting SMBHs can regulate the growth of the black holes as well as the evolution of their host galaxies, making feedback a potentially important piece of the theory of SMBH-host galaxy co-evolution (e.g. Di Matteo et al. 2005; Springel et al. 2005; Di Matteo et al. 2007; Sijacki et al. 2007).

Building up the mass of a galaxy and driving AGN feedback requires a continuous replenishment of fuel in the center of the galaxy. A comprehensive understanding of such fueling is not possible without detailed knowledge about matter transport from large scales to the vicinity of the black hole. That transport helps determine, in particular, both the amount of material available for accretion, feedback, and star formation, as well as the strength and duration of the fueling. Large scale gravitational tidal fields created during major mergers of galaxies are thought to be effective at funneling matter toward the centers of galaxies. Indeed, simula-

tions and semi-analytic modeling of hierarchical growth scenarios have shown that a combination of accretion and black hole mergers can effectively build-up the local black hole population (Kauffmann & Haehnelt 2000; Yoo & Miralda-Escudé 2004; Volonteri & Rees 2005; Malbon et al. 2006; Volonteri & Rees 2006; Li et al. 2007), as well as assemble the $\sim 10^9 M_\odot$ black holes already observed to be present in quasars at $z \approx 6$ (Fan et al. 2003; Li et al. 2007).

Secular evolution of galaxies, particularly in the absence of major merger events, can drive fuel down to the center as well. Global bar instabilities are thought to be efficient at transporting angular momentum, allowing material in the disk to move toward the center of the galaxy (Roberts et al. 1979; Simkin et al. 1980; Noguchi 1988; Shlosman et al. 1989; Kormendy & Kennicutt 2004; Regan & Teuben 2004). In the “bars within bars” scenario of Shlosman et al. (1989), a large scale galactic bar drives gas inward where it forms a self-gravitating disk. As this disk becomes unstable, a smaller secondary bar forms, driving material down to scales of order 10 pc, at which point other physics can take over and transport the material the rest of the way toward the black hole (e.g. Shlosman et al. 1990).

Given the complexity of transporting matter from cosmological scales all the way down to the circumnuclear region of a galaxy, and ultimately to the vicinity of a SMBH, it is clear that a thorough understanding of the relationship between SMBHs and galaxy formation requires modeling of a wide range of scales. Recently, cosmological SPH simulations have been combined with smaller scale simulations of a SMBH host galaxy environment to study the effects of merger driven fueling and AGN feedback on supermassive black hole growth and demography (Di Matteo et al. 2007; Sijacki et al. 2007). Reaching a large dynamic range in N-body+SPH simulations, Mayer et al. (2007) have studied galaxy dynamics during mergers resulting in a supermassive black hole binary. Small scale simulations have addressed gas dy-

¹ JILA, University of Colorado, Boulder, CO 80309; robyn.levine@colorado.edu

² Department of Astrophysical & Planetary Sciences, University of Colorado, Boulder, CO 80309, USA

³ Particle Astrophysics Center, Fermi National Accelerator Laboratory, Batavia, IL 60510, USA

⁴ Kavli Institute for Cosmological Physics, The University of Chicago, Chicago, IL 60637, USA

⁵ Department of Astronomy & Astrophysics, The University of Chicago, Chicago, IL 60637, USA

⁶ Enrico Fermi Institute, The University of Chicago, Chicago, IL 60637, USA

namics in sub-galactic scale disks with high resolution (Fukuda et al. 2000; Wada 2001; Wada & Norman 2001; Escala 2007; Wada & Norman 2007), finding the development of a turbulent, multi-phase interstellar medium (ISM).

The study we present here follows the evolution of the circumnuclear region in a typical galaxy environment rather than a dramatic, rare event such as a major merger, in a self-consistent cosmological simulation. We have specifically chosen a simulated galaxy that will evolve into a typical L_* galaxy at $z = 0$. The simulation follows the galaxy during a phase of its evolution in which it has not undergone any major mergers within several dynamical time scales, in order to follow the development of instabilities in the circumnuclear disk, which may drive the transport of matter and angular momentum from large to small scales. The cosmological simulations use the adaptive mesh refinement (AMR) technique to self-consistently model the gas dynamics in a single galaxy at high resolution (sub-pc resolution in the center of the galaxy). A large dynamic range (> 10 million), achievable with AMR technique, allows us to bridge cosmological scales to scales relevant for molecular cloud formation (the birthplace of stars) and AGN fueling. After studying the physics in this basic model galaxy, we can begin to include physical processes that are directly relevant to the problem of SMBH growth in the context of galaxy evolution, such as AGN feedback.

It is a complex task to implement mergers, feedback and secular evolution in large, cosmological simulations all at once. Our approach is to split the problem into pieces to be addressed one at a time, ultimately building a more realistic simulation. While the present paper focuses on the structure of the galaxy, and the development of instabilities which may be responsible for driving matter and angular momentum transport within the galaxy, we plan to explore the time evolution of such transport, specifically the evolution of the accretion rates of mass and angular momentum, in a subsequent paper. The nature of the circumnuclear region and a quantitative analysis of accretion rates each have important consequences for galaxy evolution.

The organization of the paper is as follows. In Section 2, we describe the details of the simulation and the adopted “zoom-in” method. In Section 3, we describe the features of the highly-resolved galaxy in a single zoom-in episode at $z = 4$, including a stability analysis of the disk and the potential role of physics not included in the current simulation. Section 4 examines the potential role of physics missing from the simulations. Finally, Section 5 contains a summary of our conclusions and their interpretation.

2. SIMULATION

Sections 2.1 and 2.2 briefly explain details of the simulation and of our methods. Additional details regarding tests of angular momentum conservation, and the treatment of dark matter particle discreteness effects will be available in the PhD thesis of the author Levine (also see the discussion of angular momentum conservation in Appendix B).

2.1. *Simulation Code*

It is unfeasible to follow the evolution of a galaxy all the way down to the scale of a black hole hole accretion disk over cosmological times. Such a simulation spans a large range of scales (with a dynamic range $> 10^7$), and each spatial scale has a different temporal scale. As a result, the Courant condition for numerical stability requires very small time steps in the most highly refined regions, making it computationally expensive to follow the evolution of the galaxy over long periods of time. It is much more feasible to start with a lower resolution cosmological simulation, and zoom in to the small-scale region with increasingly smaller cell sizes and time steps. As the simulation evolves on small scales, the large scale portion of the simulation does not undergo much evolution, and does not need as high resolution.

The cosmological simulations presented in this paper are conducted with the Adaptive Refinement Tree (ART) code (Kravtsov et al. 1997; Kravtsov 1999; Kravtsov et al. 2002). The ART code includes the technique of adaptive mesh refinement (AMR), allowing high resolution of a galaxy residing in a small region of the cosmological simulation, while following the rest of the simulated region with lower resolution. The technique is appropriate for studying the structure and evolution of a galaxy over a large dynamical range and in a cosmological context.

The ART code includes a range of physics for modeling dark matter, stars, and gas dynamics. Gas is converted into stars in cells with densities greater than ρ_{SF} and temperatures less than T_{SF} , where $\rho_{SF} = 1.64 \text{ M}_\odot \text{ pc}^{-3}$ and $T_{SF} = 9000 \text{ K}$ (see Kravtsov 2003, for more details), resulting in a star formation efficiency consistent with a Kennicutt law on kiloparsec scales (Kennicutt 1998) and with observations on 100 pc scales as well (e.g. Young et al. 1996; Wong & Blitz 2002). The code follows ISM physics, such as molecular hydrogen formation, and gas cooling by heavy elements and dust under the assumption of collisional ionization equilibrium. The cooling and heating rates are tabulated as functions of gas density, temperature, metallicity, and redshift over the temperature range $10^2 < T < 10^9 \text{ K}$ using CLOUDY (Ferland et al. 1998), which accounts for the metallicity of the gas, and formation of molecular hydrogen and cosmic dust. In future studies, we plan to include the ART code’s radiative transfer capabilities, which will be necessary for implementing AGN feedback.

2.2. *“Zooming-In” to the Center of a Galaxy*

We begin with a cosmological simulation, evolved from a realization of a random Gaussian density field at $z = 50$, with periodic boundary conditions, measuring $6h^{-1}$ comoving Mpc across. The simulation was first run with low-resolution in order to select a galactic-mass halo for subsequent study. A Lagrangian region the size of five virial radii of the halo at $z = 0$ was then identified at $z = 50$, and re-sampled and run with higher resolution to $z = 2.8$ (see Klypin et al. 2001, for a description of the technique). The Lagrangian region of the simulation was automatically refined three levels, as a minimum. There are 2.64×10^6 dark matter particles in the Lagrangian region, each with mass $9.18 \times 10^5 h^{-1} \text{ M}_\odot$. Subsequent refinement and de-refinement in this region followed a dark matter mass criterion, in which a cell was refined if its total dark matter mass is greater than $1.8 \times 10^6 h^{-1} \text{ M}_\odot$.

At $z = 4$, the highest matter density peaks in the simulation have a maximum resolution of ≈ 50 pc (in physical units; corresponding to 9 levels of refinement on top of a 64^3 root grid). The largest halo has a total mass of $2 \times 10^{11} M_\odot$ at $z = 4$, and it contains the progenitor of an L^* spiral galaxy. This initial cosmological simulation was run including metal enrichment and energy feedback from supernova, and radiative transfer in addition to the physics described in Section 2.1.

This particular $z = 4$ cosmological simulation was chosen for this study because it contains a galaxy that has not been disturbed by a major merger since it merged with a galaxy with 25% its mass at $z \approx 6$. The time since this dynamically active period (≈ 600 million years) is significantly longer than the dynamical time of the galactic disk at $z \approx 4$ (≈ 15 million years). The galaxy is, however, far from quiescent, having grown in mass by $\approx 25\%$ from $z = 5$ to $z = 4$ via minor mergers and accretion from its environment.

In the cosmological simulation, we allow further refinement (at $z \approx 4$), one level at a time, in a 1.5 kpc region centered on the galaxy, effectively zooming in to the center of the galaxy with increasing resolution. The “zoom-in” technique is similar to the one used by Abel et al. (2002) in simulations of the formation of the first star, which required an even larger dynamical range. Because we are starting simply in this first pilot study, and building a more realistic simulation in pieces, radiative transfer and stellar feedback have been switched off in the zoom-in portion of the cosmological simulation (they will be examined in future studies). The high-resolution portion of the simulation employs additional refinement criteria, refining according to a level-dependent mass criterion on levels 11 and below⁷ in the zoom-in region. The refinement criterion is defined so that the finer the resolution, the more aggressively the mesh refines, ensuring that there are enough highly refined cells to resolve structures on small scales. Specifically, the mesh refinement is super-Lagrangian in the circumnuclear region of the galaxy, and cells are marked for refinement if the gas mass in a cell is $m_r^{\text{level}-10}$ times the Lagrangian mass criterion ($9 \times 10^7 h^{-1} M_\odot$), where $m_r = 0.7$ is our fiducial value. The factor 0.7 was chosen through experimentation, so as to make the refinement in the central region more aggressive, but not so aggressive that the simulation becomes too computationally expensive.

During the zoom-in period, we increase the maximum level of refinement gradually, one level at a time, allowing the simulation to reach a quasi-stationary state on each level before moving to the next. The slow initial refinement allows the ART code to resolve spatial scales within the simulated galaxy while avoiding transient effects. Since the time steps depend on the sound speed of the gas, they are therefore related to the dynamical time, and a fixed minimum number of time steps on each level forces the mesh to evolve for several dynamical times. We have run parallel simulations with 100, 300, and 1000 minimum steps on each level, and have determined that a requirement of a minimum of 300 on each level suf-

ficiently reduces transient numerical effects that result from refining too quickly.

Throughout the initial zoom-in, we take precautions to avoid numerical artifacts. As the resolution of the simulation increases and throughout its subsequent evolution, the density of dark matter is smoothed on scales corresponding to level 9 resolution and above. This ensures that each cell contains $\approx 15 - 20$ dark matter particles, avoiding effects resulting from their discreteness. It is well known that poor resolution in hydrodynamics codes can lead to artificial fragmentation in the gas. Truelove et al. (1997) investigated these numerical instabilities and found that a simulation must resolve the Jeans length to avoid artificial fragmentation. In addition to the mass criteria described above, the ART code’s refinement scheme meets the Jeans condition of Truelove et al. (1997) on the maximum level of refinement (which increases gradually during the initial zoom-in episode), requiring that $\Delta x / \lambda_J < 0.25$, where Δx is the resolution, or cell size, and λ_J is the Jeans length. Additionally, as the mesh refines, rapidly collapsing structures can cause numerical instabilities at steep density gradients. The ART code implements artificial pressure support (as described in Machacek et al. (2001)) on the maximum level of refinement, in order to avoid the over-collapsing of structures.

After the initial zoom-in, the highest level cells are 0.03 pc across (corresponding to 20 levels of refinement), allowing us to determine the location for a supermassive black hole test particle with high precision, but without resolving the black hole accretion disk, which would require additional physics (such as magnetohydrodynamics, or MHD) not currently included in the ART code. Our results extend reliably down to a scale of at least 0.12 pc, or the size of four level 20 cells, which we consider to be our resolution limit. After reaching this maximum resolution (level 20), we replace $3 \times 10^7 M_\odot$ of the gas from the center of the simulated galaxy with a black hole point mass of equal mass and momentum. At present, we focus on the dynamical properties of the circumnuclear disk on scales where the gravity of the gas dominates that of the black hole. The addition of the black hole point mass here simply allows us to follow the black hole’s location and velocity as a reference point. However the successful introduction of the black hole particle will be essential in subsequent simulations involving physics associated with the black hole (such as AGN feedback).

After the initial zoom-in and the successful introduction of the black hole test particle, the simulation then evolves at high resolution for approximately one dynamical time at the 100 pc scale, showing a highly resolved galactic disk. For a quasi-Keplerian disk, the number of orbital periods, N_{orb} , undergone by the simulation at radii less than 100 pc, is $(R/100 \text{ pc})^{-3/2}$. Figure 1 shows the 3-dimensional gas density in an approximately face-on view of the galactic disk, on several different spatial scales, for a single time step, demonstrating the large dynamic range of the simulation. The distribution of stars is shown in Figure 2, in both a face-on and an edge-on view of the galaxy on a scale of 3 kpc. The two different colors correspond to old and young stars (yellow and blue, respectively), with the youngest stars in the

⁷ It should be noted that we adopt the convention of referring to level 0 as the “top” level, and the maximum (most-refined) level as the “bottom” level, so that the terms “above” and “below” refer to lower and higher resolution, respectively.

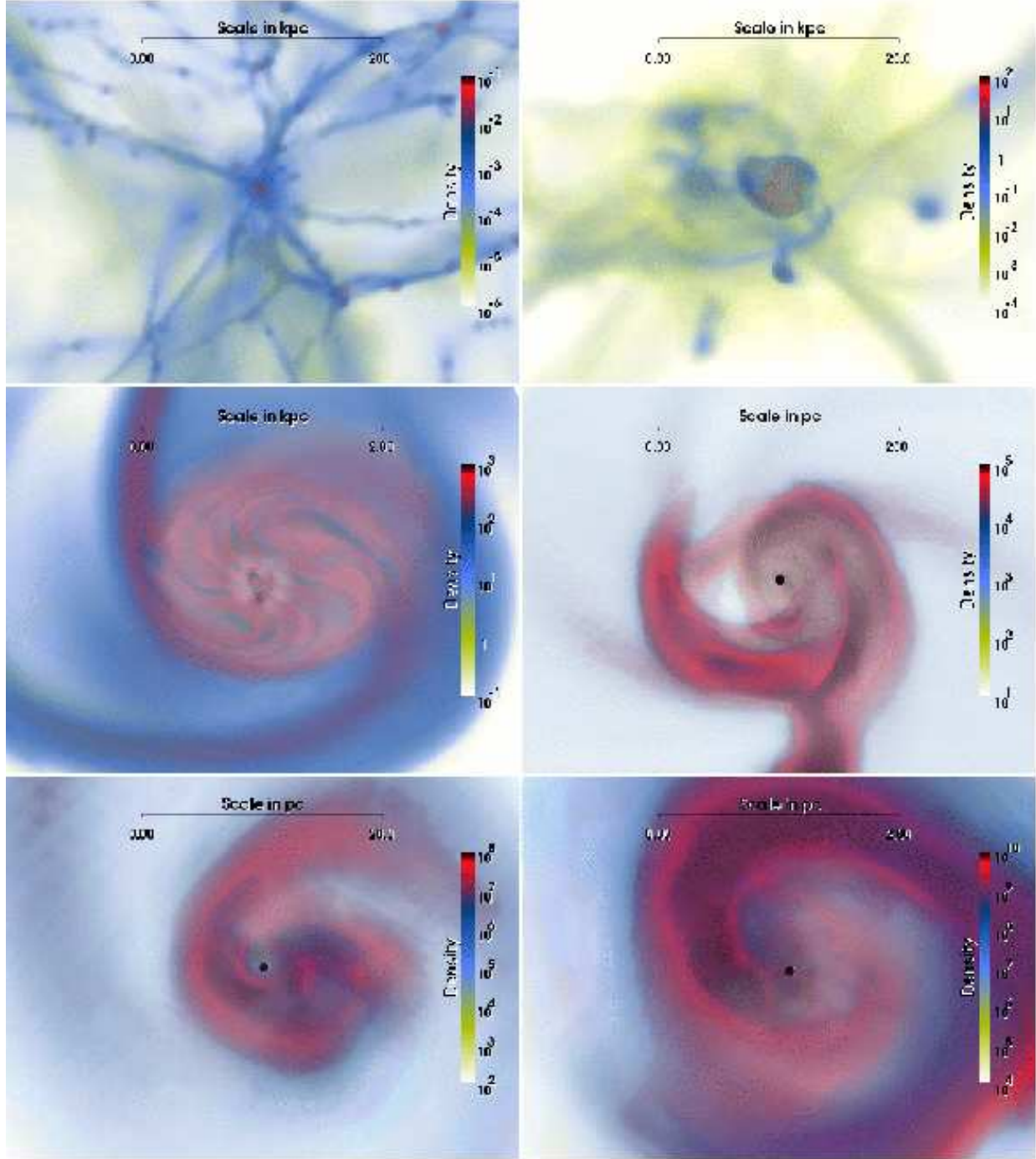


FIG. 1.— Volume rendering of the 3-dimensional gas density on several different scales at $z = 4$, from 200 kpc in the upper left panel, to 2 pc in the lower right panel. The color bar shows the density scale in units of cm^{-3} . Note the presence of the spiral arms and instabilities on a wide range of scales. (This figure is best viewed in color.)

galaxy located primarily in the disk, and the oldest stars distributed more isotropically, populating the galaxy's bulge.

3. RESULTS

3.1. Structure of the Circumnuclear Disk

Volume rendered images of the gas density in the $z = 4$ simulation, such as those in Figure 1, clearly show the spiral disk structure of the galaxy. The gas disk extends inward all the way to sub-pc scales, which are the small-

est scales resolved in our simulation⁸. The geometric structure of the circumnuclear region is best illustrated by the eigenvalues of the inertia tensor, calculated in spherical shells around the black hole. The inertia tensor is given by

⁸ In particular, the simulated disk does not contain the commonly observed toroidal structure in the inner few pc of the galaxy. The failure of our simulation to reproduce the AGN torus may be the result of additional physics still missing in the simulation, as we will discuss in §4.1.

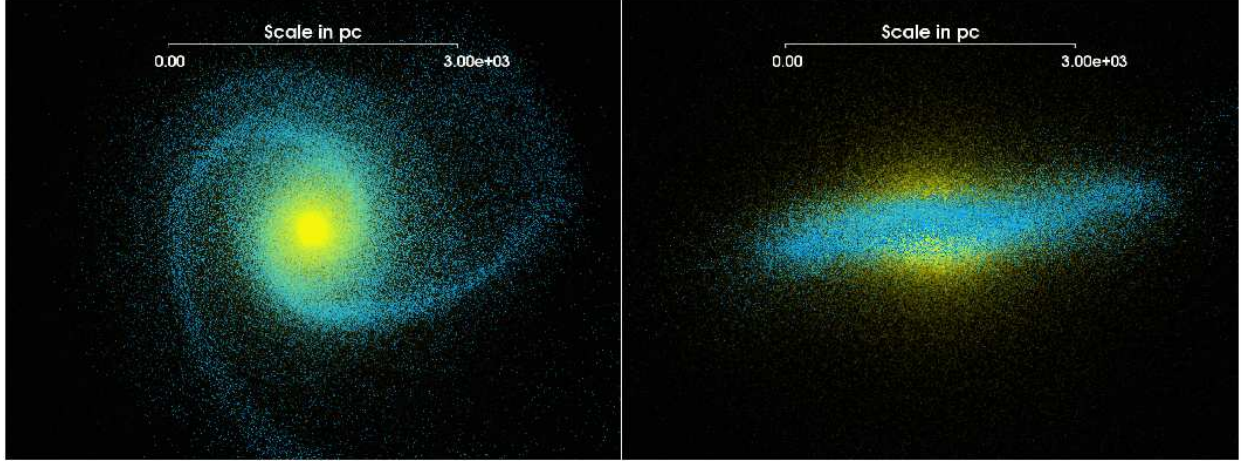


FIG. 2.— The stellar component of the galaxy at $z = 4$ on a scale of 3 kpc. The stars in the image are divided into two populations, with yellow stars corresponding to the oldest stars in the galaxy, and blue stars corresponding to the youngest stars. The youngest stars are found primarily in the disk of the galaxy. (This figure is best viewed in color.)

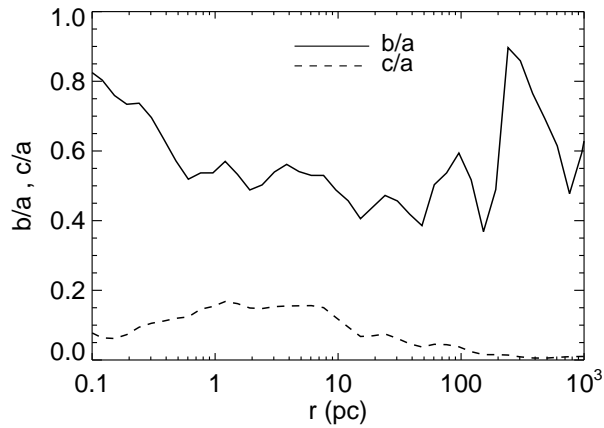


FIG. 3.— Ratios of eigenvalues of the inertia tensor in spherical shells centered on the black hole. The ratio $c/a \ll b/a$, indicating a disk structure.

$$I_{jk} = \sum_{\alpha=1}^N m_\alpha x_j^\alpha x_k^\alpha, \quad (1)$$

where m_α is the gas mass of cell α at radius $r_\alpha = |\mathbf{x}_\alpha|$ inside a spherical shell containing N cells, and centered on the black hole. The eigenvalues of the inertia tensor define the principal axes of each shell, and their ratios describe the shape. Figure 3 shows the average radial profile of the ratios of the inertia tensor's eigenvalues. Above 0.1 pc, c is significantly smaller than b over several orders of magnitude in radius, indicating a disk structure. However, the fact that b/a is significantly less than one in parts of the disk indicates that the disk is not axially symmetric, and that it has large-scale structures, such as spiral waves and bars.

The gas disk in the simulation is fully rotationally supported, with the tangential component of velocity dominating over the radial component by at least an order of magnitude, as is illustrated in Figure 4. The top panel of Figure 4 shows the ratio of the radial to the tangential component of velocity, which is small throughout much of the disk, as the motion of the gas is almost entirely rota-

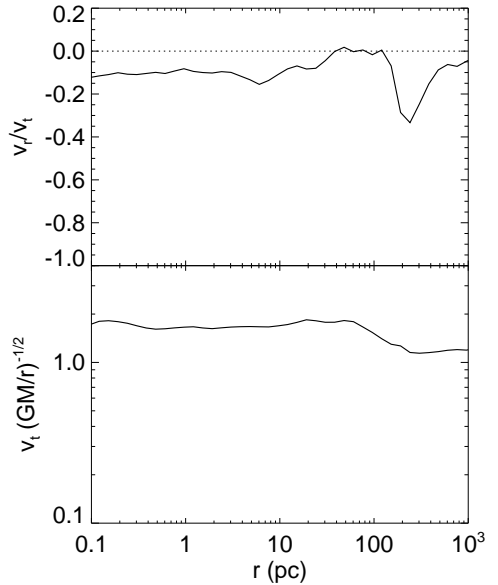


FIG. 4.— Top: Ratio of radial and tangential velocity components of the gas, each averaged over 550,000 years. Bottom: Average tangential velocity component in units of the average quasi-Keplerian velocity.

tional. The average radial velocity is negative, indicating the inflow of gas. The bottom panel shows the tangential component of velocity in units of a quasi-Keplerian velocity, $\sqrt{GM(r)/r}$, determined by the interior total mass, $M(r)$, at each radius. The velocity is close to being Keplerian, but since the mass distribution in the disk resembles a flattened ellipsoid, rather than a spherical distribution, the rotation is slightly super-Keplerian.

A remarkable feature of the circumnuclear disk is that the average gas density profile, measured within spherical shells centered on the black hole, follows an almost perfect power-law with little evolution in time. Figure 5 shows the gas density profile from two different snapshots of the simulation, as well as the average of the profile over a $\approx 550,000$ year period. Both the snapshots and the average profiles of the gas density increase by ≈ 8 orders of magnitude in the inner 100 pc of the

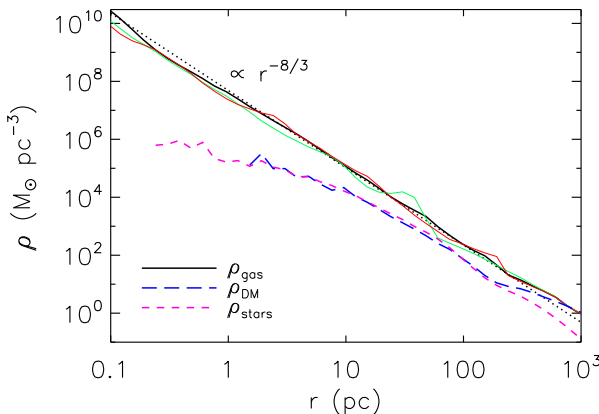


FIG. 5.— Radial profiles of the gas, dark matter, and stellar mass density. Snapshots of the gas density are shown at 100,000 and 500,000 years after the initial refinement (thin solid lines; green and red respectively, in the color version), in addition to a 550,000 year average (thick solid line). The snapshots do not show much variation from the averaged profile, demonstrating that on timescales of several hundred thousand years, the disk is in a quasi-stationary state. The dotted line shows a power-law with slope $-8/3$ for comparison, which matches the gas density slope well. The dark matter and stellar mass density profiles are shown by the long-dashed (blue in the color version) and short-dashed (magenta in the color version) lines, respectively. In the inner ~ 200 pc, the slope of the dark matter and stellar density profiles is ~ -2 consistent with the adiabatic contraction model.

simulation, obeying a steep power-law with slope $-8/3$. The stability of the gas density profile indicates that the disk is in a quasi-stationary state on timescales of several hundred thousand years. Figure 5 also shows the dark matter and stellar mass density profiles. In the central kiloparsec of the galaxy, gas comprises $\sim 62\%$ of the mass ($\sim 2.3 \times 10^{10} h^{-1} M_\odot$ total in the central kpc), dominating the dynamics of the disk. In contrast, the stellar and dark matter populations comprise ~ 13 and $\sim 25\%$ of the galaxy's mass inside the central kiloparsec. The disk is extremely gas rich at $z = 4$, because the galaxy is still actively growing and has not yet formed all of its stars. Interestingly, we find that both the stellar and dark matter profiles measured in the central ~ 200 pc of the galaxy follow simple $\propto r^{-2}$ power-laws. The profiles match those predicted for the adiabatic contraction of dark matter from an NFW profile (Navarro et al. 1997), using the model of Gnedin et al. (2004), all the way down to the 1 pc scale.

Figure 6 shows that the RMS velocity dispersion of the gas (measured between neighboring cells, and therefore depending on the resolution) greatly exceeds the sound speed in the inner 100 pc, indicating supersonic turbulence in the disk. Supersonic turbulence decays on a dynamical time scale, so the persistence of the turbulence in the circumnuclear disk of the galaxy indicates a driving mechanism, which will be addressed in the following sections. The mean sound speed of the gas indicates a cold, molecular gas disk within the central 100 pc of the simulated galaxy. The floor in the sound speed shown in Figure 6 is determined by the minimum temperature to which our adopted cooling rates (computed using the CLOUDY package) apply. The mean sound speed is computed for cells with $T < 20,000$ K, because the spherical averages shown in Figure 6 include the low density

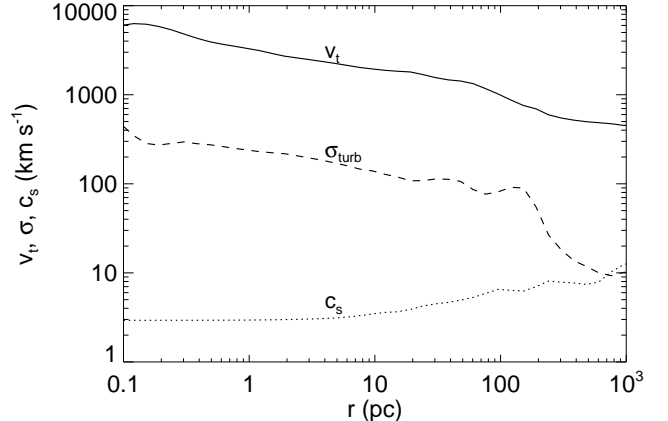


FIG. 6.— A comparison of the radial profiles of the tangential velocity component of the gas (solid), its RMS velocity dispersion, or turbulent velocity (dashed), and the mean sound speed, computed in cells with $T < 20,000$ K (dotted), time averaged over 550,000 years. The sound speed is low, indicating cold, molecular gas within the central 20 pc.

gas, infalling perpendicular to the plane of the galactic disk, and shock-heated to high temperatures ($\gtrsim 10^6$ K). Additionally, turbulence inside the disk produces localized shocks that briefly heat individual cells to similarly high temperatures. The inclusion of shock-heated gas produces a broad temperature distribution and raises the mean temperature of the gas so that it does not effectively describe the typical sound speed of the gas in the disk. Therefore, the mean is computed over a temperature range that selects cells in the disk, while excluding atypical cells, resulting in a more representative quantity for describing the thermal properties of the disk.

3.2. Angular Momentum Transport

The gas density profile of Figure 5 motivates a simple analytic description of angular momentum transport in the disk. Averaged over a sufficiently long time, the disk can be considered to be approximately azimuthally symmetric. Additionally, the rotational velocity of the disk dominates over other velocity components: over the local velocity dispersion, and over the sound speed, as demonstrated in Figure 6. Therefore, the circumnuclear disk in the simulation is well approximated by a thin, rotationally supported, viscous, molecular gas disk. Conservation of angular momentum in such a disk is described by the following equation in cylindrical coordinates (Pringle 1981):

$$\frac{\partial}{\partial t}(J_z) + \frac{1}{R} \frac{\partial}{\partial R}(Rv_R J_z) = \frac{1}{2\pi R} \frac{\partial G}{\partial R}, \quad (2)$$

where the angular momentum density normal to the disk is given by $J_z = \Sigma R^2 \Omega$, where $\Omega = v_t/R$. The surface density of the gas is Σ , and v_R is the radial component of velocity, which is small compared to the rotational velocity of the gas. The right hand side of equation (2) describes the effects of a viscous torque, G , generated by turbulent motions of the gas. Pringle (1981) parameterizes the viscous torque G , which necessarily vanishes in solid body rotation, $\partial\Omega/\partial R = 0$, as

$$G(R, t) = 2\pi\nu\Sigma R^3 \frac{\partial\Omega}{\partial R} \quad (3)$$

where ν is the coefficient of turbulent viscosity. During the initial zoom-in, the gas disk quickly reaches the power-law density profile shown in Figure 5. On short time scales of a few hundred thousand years, traced by a single high-resolution zoom-in episode of our simulation, time-averaged radial motions through the disk are small compared to the rotational motion, as shown in Figure 4. Over longer time scales, angular momentum is transported outward by a viscous torque driven by the turbulent motions of the gas, allowing accretion to slowly feed the black hole. The left hand side of equation (2) can therefore be considered to be small on time scales of a few hundred thousand years. It then follows that the right hand side of equation (2) should also be small, and that the torque G is approximately constant with radius.

Given that the gas density ρ follows a power law (Figure 5), it is reasonable to approximate the surface density of the gas Σ by a power law with the radius R :

$$\Sigma \propto R^{-\beta}. \quad (4)$$

Since the gravitational potential Φ satisfies $\nabla^2\Phi = 4\pi G\rho$ and $\Sigma = 2\rho R$, it follows that

$$\Phi \propto R^{1-\beta}. \quad (5)$$

Since the disk is almost entirely rotationally supported, the tangential velocity v_t is effectively the circular velocity v_c , defined by $v_c^2 = R d\Phi/dR$. Thus, the angular speed is

$$\Omega = \frac{1}{R} \left(R \frac{d\Phi}{dR} \right)^{1/2} \propto R^{-(1+\beta)/2}, \quad (6)$$

and the viscous torque

$$G \propto R^{3(1-\beta)/2}\nu. \quad (7)$$

If $\nu \propto R$ (which, as we will show in Section 3.3, is the case in our simulations), then equation (7) implies a power-law slope of $\beta \approx 5/3$. It then follows that the volume density of the gas should scale as $\rho \propto R^{-8/3}$, consistent with the slope measured in Figure 5. Therefore, the simple description of angular momentum transport, maintained by turbulence in the disk, potentially provides a consistent interpretation of the power-law slope of the gas density profile of Figure 5.

3.3. Disk Stability and the Source of Turbulence

In Section 3.1, we showed that the simulated galaxy contains a self-gravitating, turbulent, cold, molecular gas disk within the central ≈ 100 pc. Such disks are susceptible to instabilities and to fragmentation. In the snapshots shown in Figure 7, the presence of instabilities is illustrated by waves moving through the simulated disk. The snapshots trace the evolution of disk structure on scales of ≈ 125 pc, and ≈ 12.5 pc (inset). The rotational period of the disk at the outer radius is such that the disk has undergone at least one full rotation (several more at smaller radii) over the time scales followed by the present simulation. The panels show the somewhat chaotic formation and re-formation of spiral structures

on these scales, in contrast with the more ordered spiral structure seen on kiloparsec scales (Figure 1). This section includes an analysis of the behavior of structures in the disk on the scales shown in Figure 7.

The Toomre Q parameter describes the stability of the disk against linear perturbations, and is given by $Q = \sigma_{\text{turb}}\kappa/\pi G\Sigma$, where κ is the epicyclic frequency, and Σ is the surface density of the gas, both determined locally (Toomre 1964; Goldreich & Lynden-Bell 1965). Although the disk is cold, and the sound speed is low, the RMS velocity dispersion is substantially higher than the sound speed inside 100 pc, indicating that the gas is turbulent. Therefore, in place of the sound speed typically used in the definition of the Toomre Q parameter, we have substituted a turbulent velocity, given by the quadrature sum of the sound speed and the RMS velocity dispersion of the gas. The disk is, for the most part, quasi-Keplerian (as described in Section 3.1), so that the epicyclic frequency κ is proportional to the angular speed of the disk, $\Omega = v_t/r$.

The top panel of Figure 8 shows the Toomre Q parameter for the simulated disk, corresponding to the region shown in Figure 7. Where $Q < 1$, the disk is susceptible to local gravitational instabilities resulting from axisymmetric perturbations. For $Q > 1$ the disk is likely to be stable against axisymmetric perturbations, but is still susceptible to instabilities arising from non-axisymmetric perturbations, which are less stable than radial perturbations (Polyachenko et al. 1997). For the density profile shown in Figure 5, the disk becomes stable for $Q \gtrsim 2$. The shaded region in Figure 8 ($1 < Q < 2$) therefore represents marginally stable values of the Q parameter, where the disk still might become unstable. Figure 8 suggests that the disk in the simulated galaxy lies mostly in the region of marginal stability inside ≈ 1 kpc. In the case of axisymmetric perturbations, the fastest growing unstable mode corresponds to the scale $\lambda_{\text{fast,r}}$, at which $d\omega^2/dk = 0$ (where ω is the angular frequency of waves in the disk), given by

$$\lambda_{\text{fast,r}} = \frac{2\sigma_{\text{turb}}^2}{G\Sigma}. \quad (8)$$

Using the condition for marginal stability from Polyachenko et al. (1997), the fastest growing mode for all modes (axisymmetric and non-axisymmetric), $\lambda_{\text{fast,all}}$, is given by

$$\lambda_{\text{fast,all}} = \frac{\lambda_{\text{fast,r}}}{2} = \frac{\sigma_{\text{turb}}^2}{G\Sigma}. \quad (9)$$

The bottom panel of Figure 8 shows the ratio λ/r for each of the fastest growing modes. In the inner 100 pc, the scales of the fastest growing modes are smaller than the radius by only a factor of a few, implying that the disk is stable on scales $\lambda \ll R$ (at least in the linear regime). This is an indication that perturbations in the disk operate on a range of scales, but always on scales that are an appreciable fraction of the size of the system, driving global instabilities, which generate turbulence on smaller scales. The disk remains locally stable all the way into a region less than 1 pc from the black hole. There is no catastrophic fragmentation into clumps small enough to form stars, so that angular momentum transport may continue uninterrupted by bursts of star formation.

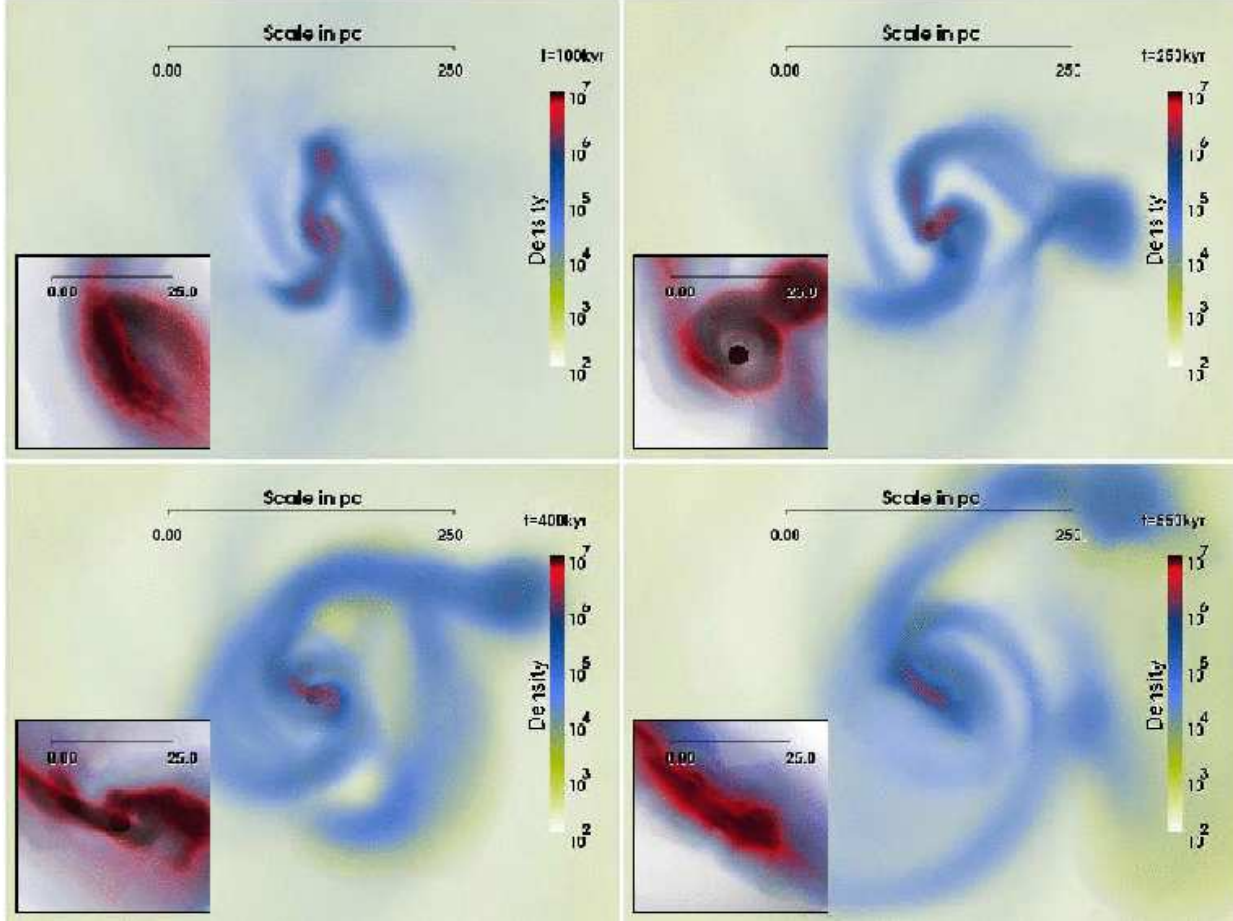


FIG. 7.— The evolution of global instabilities in the disk over time, on a scale of ≈ 125 pc and on a scale of ≈ 12.5 pc (inset). Each panel shows a volume rendering of the gas density (in cm^{-3}) at a different epoch. The similarities between the appearance of the disk on the two different scales indicate the hierarchical structure of the disk. (This figure is best viewed in color.)

By dimensional analysis, the turbulent kinematic viscosity ν discussed in Section 3.2 can be described by $\lambda\sigma_{\text{turb}}$, where λ is a characteristic scale for turbulence and σ_{turb} , the turbulent velocity shown in Figure 6, is a characteristic velocity. It is natural to identify the characteristic length scale with the length scale corresponding to the fastest growing unstable mode, $\lambda_{\text{fast},r}$, so that $\nu \sim \lambda_{\text{fast},r}\sigma_{\text{turb}}$. The top panel of Figure 9 shows that the turbulent viscosity ν , given approximately by $\lambda_{\text{fast},r}\sigma_{\text{turb}}$, scales linearly with the radius over much of the disk, so that $\nu \propto R$. Although the behavior of the turbulent viscosity ν can potentially change with time, the viscous torque G should remain approximately constant in radius for the above interpretation to be valid. The bottom panel of Figure 9 shows the average viscous torque G , normalized to its value at 10 pc. The normalized value is close to unity over most of the circumnuclear region, which is indeed the condition needed to explain the $-8/3$ slope of the spherically-averaged gas density profile of Figure 5.

Thus, a simple description of the structure of the circumnuclear disk based on equations (2-7) and Fig. 9 provides a good match to the simulation results, supporting the idea that global instabilities in the disk are responsible for generating turbulence in the gas, resulting in the power-law slope described in Sections 3.1 and 3.2.

The conditions in the circumnuclear disk are poten-

tially conducive to gaseous bar formation, the conditions for which have been studied extensively for different geometries and physical conditions, resulting in a variety of criteria (e.g. Ostriker & Peebles 1973; Efstathiou et al. 1982; Christodoulou et al. 1995a,b; Bottema 2003; Wyse 2004). A comparison with the criterion of Ostriker & Peebles (1973), which characterizes stability in terms of the ratio $t = T/|W|$ of kinetic to gravitational potential energy, indicates that the disk is both secularly and dynamically unstable to bar formation on all scales $r \gtrsim 0.1$ pc adequately resolved by the simulation. Because of the chaotic and transient behavior of the instabilities, the structures shown in Figure 7 do not resemble a single, well defined bar, but rather a highly perturbed “bar.”

Since the Toomre criterion applies only to small linear perturbations and the Ostriker-Peebles criterion describes global modes, the question remains whether non-linear effects lead to fragmentation on smaller scales, below the resolution of the simulation. The top panel of Figure 10 shows the ratio of the local Jeans length of the gas, λ_J , to cell size, Δx , for all simulation cells in the circumnuclear disk (with temperatures less than 10^3 K). In most cells, the Jeans length is larger than the cell size, preventing the gas from fragmenting into sub-cell sized clouds, ultimately leading to star formation. The Truelove criterion for preventing numerical fragmentation is

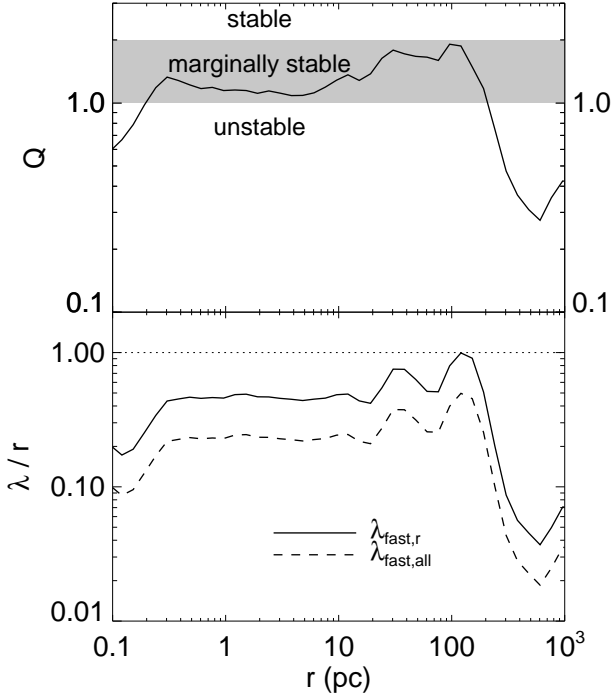


FIG. 8.— *Top:* Toomre Q parameter. For $Q < 1$ the disk is unstable, and for $Q \gtrsim 2$ the disk is stable. In the regime $1 < Q < 2$, the disk is marginally stable (stable against axisymmetric modes, but not non-axisymmetric modes). *Bottom:* Average values of the fastest growing unstable mode for axisymmetric perturbations, $\lambda_{\text{fast},r}$ (*solid*), and the fastest growing unstable mode for all perturbations, $\lambda_{\text{fast},\text{all}}$ (*dashed*), each divided by radius. The ratio $\lambda/r \gtrsim 0.1$ throughout the circumnuclear disk, so there is no catastrophic fragmentation down to small scales.

enforced on the maximum level of refinement (level 20) only, so there are no numerical restrictions to prevent gas from collapsing all the way to level 20. However, only the central sub-pc part of the disk reaches levels 19 and 20, as shown by the histogram in the lower panel of Figure 10, indicating that the disk is stable to nonlinear effects. While some cells in the disk have $\lambda_J < \Delta x$ and may form stars, Figure 10 demonstrates that most of the disk is stable against collapse, and that there is no widespread burst of star formation. The few cells with $\lambda_J/\Delta x < 1$ may correspond to resonances where the pattern speed of waves in the disk is the same as the rotational velocity, leading to higher gas densities, and possible star formation. However, a detailed analysis of the behavior of these resonances with time is beyond the scope of this paper.

3.4. The Nature of the Turbulence

Turbulence has been widely studied in modeling of the ISMs of galaxies and star forming regions (for recent reviews, see Mac Low & Klessen 2004; McKee & Ostriker 2007). It is important to understand the nature of the turbulence in the present simulated galaxy as it plays a key role in the disk properties. The global instabilities arising in the simulated circumnuclear disk generate turbulence on a range of scales, maintaining the quasi-steady state of the disk.

Turbulence dissipates energy in such a way that the turbulent velocity scales as $\sigma_{\text{turb}} \propto \lambda^q$, where $q = 1/3$ for

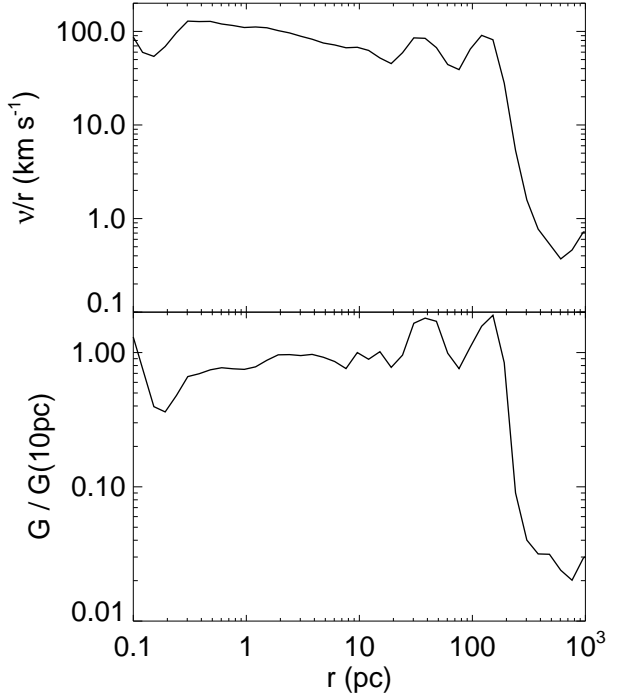


FIG. 9.— *Top:* Ratio of kinematic viscosity ν , given approximately by $\lambda_{\text{fast},r} \sigma_{\text{turb}}$, to radius R . The ratio ν/R is roughly constant in radius. *Bottom:* The viscous torque G normalized to its 10 pc value. The viscous torque is constant in radius, consistent with the power-law gas density slope $\rho \propto R^{-8/3}$.

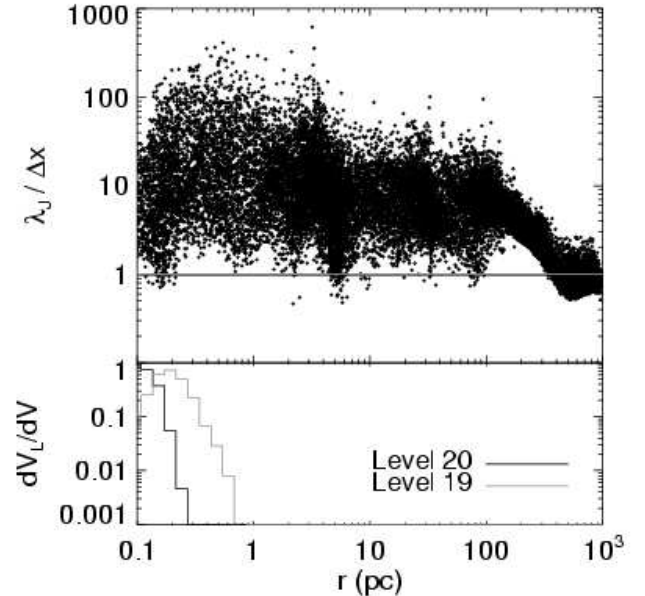


FIG. 10.— *Top:* Scatter plot showing the ratio of the local Jeans length, λ_J , to the cell size, Δx at 300,000 years after the initial refinement. Only cool cells with temperatures less than 10^3 K are shown. *Bottom:* Histogram showing the volume of level 20 and of level 19 cells as a function of radius. The simulation only refines to the maximum levels in the center of the circumnuclear disk.

incompressible, sub-sonic (Kolmogorov) turbulence and $q = 1/2$ for compressible turbulence in the zero-pressure limit (Burgers turbulence). The supersonic turbulence in the simulated disk falls between these two limits. In

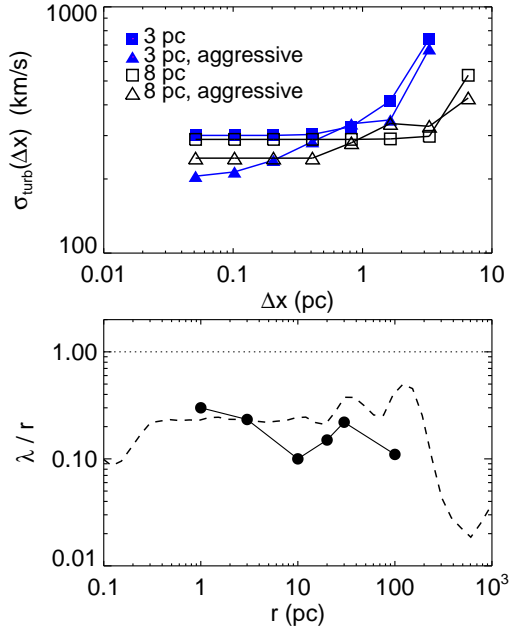


FIG. 11.— *Top:* Turbulent velocity as a function of scale (or cell size) at 3 and 8 pc, for the fiducial and aggressive refinement runs. The more aggressive refinement run resolves the scaling of the turbulence down to smaller scales. *Bottom:* A comparison of the smallest resolved scale of turbulence and the fastest growing unstable mode, $\lambda_{\text{fast},\text{all}}$ (where $\lambda_{\text{fast},\text{all}}$ is the same as in Figure 8).

AMR simulations, it is straightforward to measure the turbulent velocity on different scales because the information on different levels of refinement is readily available. However, the measurements are only accurate to within a factor of two in scale because the cell size decreases by a factor of two with each refinement. The approximate scaling of the turbulence is shown in the top panel of Figure 11. The figure shows the turbulent velocity (given by the RMS velocity dispersion between neighboring cells) at two different radii for two different simulation runs. The first is the fiducial run described in the previous sections, and the second is a short portion of the fiducial run, with a more aggressive refinement criterion on levels 13 and below, given by $m_r^{\text{level}-10} \max[0.5^{\text{level}-12}, 0.125]$ (where m_r is an empirically determined parameter defined in Section 2.2). The more aggressive run probes smaller scales at a given radius, in order to capture the scale of the turbulence. The turbulent velocities shown in Figure 11 demonstrate the scaling of the turbulence down to small scales. It is difficult to determine the precise slope of the scaling using measurements from the present simulation because of the limitation imposed by the refinement scheme. While a more precise characterization of the turbulence spectrum is beyond the scope of the present simulation, Figure 11 shows that the slope approximately falls between the Kolmogorov and Burgers turbulence limits, as expected.

At scales below the resolution at a given location in the disk, the turbulent velocities in Figure 11 level off at constant values because the turbulence scaling can only be measured down to the resolution limit. The more aggressive refinement run (*triangles* in Figure 11) probes smaller scales for a given radius, and therefore levels off at smaller scales. The bottom panel of Figure 11

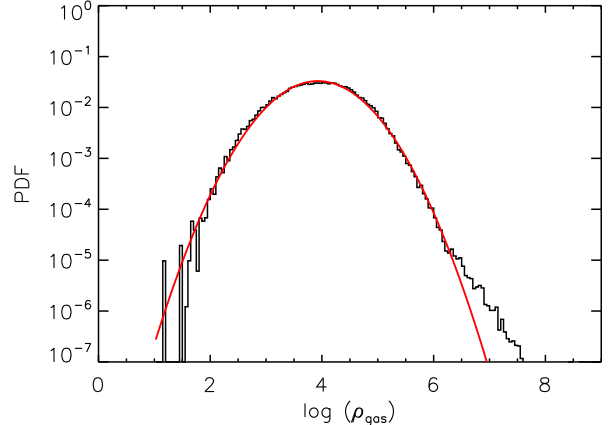


FIG. 12.— A volume-weighted PDF of the gas density in cells at a scale of ~ 30 pc, with temperatures $< 10^3$ K (in order to exclude the hot corona outside the disk), averaged over $\sim 550,000$ years. The PDF is well fit by a log-normal distribution over the range $10^2 \lesssim \rho \lesssim 10^6 M_\odot \text{ pc}^{-3}$ with a mean density of $10^{3.9} M_\odot \text{ pc}^{-3}$ (line).

shows the approximate scale at which the flattening of the spectrum occurs for several different radii in the circumnuclear disk of the fiducial run. For comparison, the fastest growing unstable mode, $\lambda_{\text{fast},\text{all}}$ is shown as well. The turbulent velocity measured at the resolution of the simulation is a numerical quantity, but it roughly corresponds to the turbulence on the scale of $\lambda_{\text{fast},r}$, which is a physical quantity. Figure 11 demonstrates that the simulation resolves all scales that are Toomre Q unstable, supporting the resulting interpretation that instability driven turbulence maintains a quasi-stationary state of the circumnuclear disk.

The density structure of the disk is also consistent with the description of turbulence in the disk. Supersonic turbulence typically imposes a log-normal density distribution on the gas, as demonstrated by models of turbulence in molecular clouds (e.g. Vazquez-Semadeni 1994; Passot & Vázquez-Semadeni 1998; Wada 2001; Krtsuk et al. 2007; McKee & Ostriker 2007), such as

$$\frac{dV}{d\rho} = \frac{1}{\rho\sqrt{2\pi\sigma^2}} \exp\left[\frac{-(\ln\rho - \mu)^2}{2\sigma^2}\right], \quad (10)$$

where the mean, μ , is defined as $\overline{\ln\rho}$, and σ is the dispersion. Figure 12 shows the volume-weighted probability distribution function (PDF), time-averaged over $\sim 250,000$ years, for a shell of gas at a radius of 30 pc. The PDF is well fit by a log-normal distribution over at least 4 orders of magnitude in density, consistent with models of supersonic turbulence.

4. POSSIBLE EFFECTS OF MISSING PHYSICS

The simulations presented here do not include all of the potentially important physics for galaxy evolution. Therefore, in this section we discuss the potential effect that the physics missing from the simulations might have on our results.

4.1. Optically Thick Cooling

Cooling in the high density, central region of the galaxy is not treated entirely correctly by the ART code. The

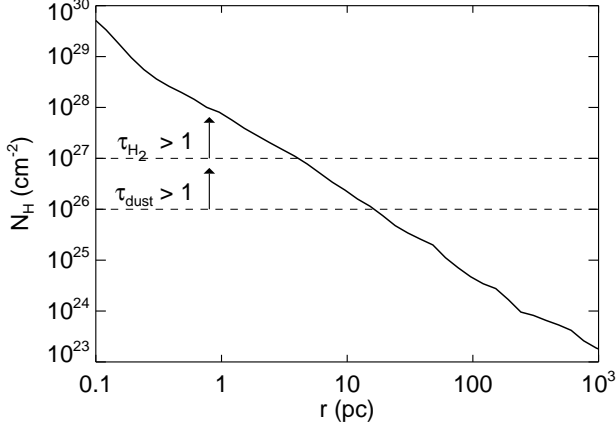


FIG. 13.— Column density of the gas. The horizontal lines show the column densities at which dust and H₂ become optically thick to their own cooling radiation.

column density of the molecular gas in the center is so high that the gas is expected to become optically thick to its own cooling radiation (e.g. Ripamonti & Abel 2004). Additionally, the presence of dust grains in this region traps radiation and halts cooling further (see Draine & Lee 1984; Ossenkopf & Henning 1994). Figure 13 shows the column density vertically through the circumnuclear gas disk. Horizontal lines are shown for comparison, corresponding to the column densities at which dust and H₂ each become optically thick to their own cooling radiation ($\sim 10^{26}$ cm⁻² and $\sim 10^{27}$ cm⁻², respectively, at 0.1 solar metallicity, which is the metallicity of the circumnuclear disk in the simulation at $z = 4$). In the inner ≈ 10 pc, the column density of the gas is large enough that the opacity of dust and molecular gas must be accounted for to accurately describe cooling in the simulation.

The simulation runs presented here do not include optically thick radiative transfer. This may explain why the gas remains in a thin disk all the way in to sub-pc scales, and does not resemble the obscuring tori observed in the inner few parsecs of AGN. Should the opacity of the gas to its own cooling radiation be included, the gas around the mid-plane of the disk would not be able to cool and would heat to temperatures corresponding to the energy dumped into the gas by the turbulence. These higher temperatures may be able to provide a substantial vertical pressure support in the central few parsecs of the disk, resulting in a thicker, more toroidal-like structure⁹. However, it has been suggested that hydromagnetic disk winds, and not hydrostatic pressure support, may be responsible for sustaining the optically and geometrically thick obscuration region, or “obscuring torus,” in the nuclei of galaxies (e.g. Konigl & Kartje 1994; Elitzur & Shlosman 2006). In which case, the inclusion of optically thick radiative transfer may not be sufficient to create a “torus” in our simulations.

In future simulations we plan to remedy this limitation of the present simulation by accounting for the opacity

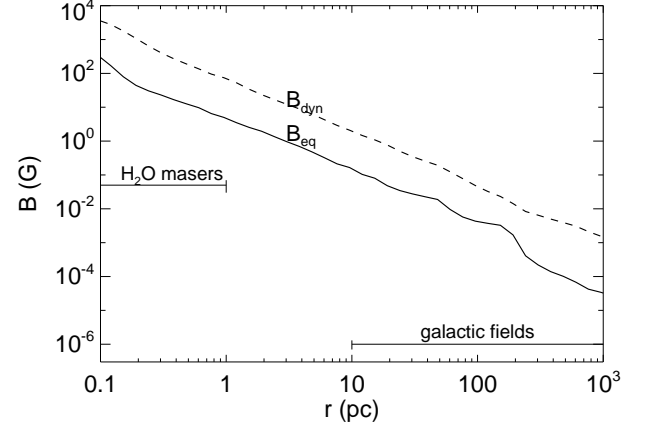


FIG. 14.— Equipartition (solid) and dynamical (dashed) magnetic fields needed to influence the gas dynamics in the disk.

of the high density region in the center, which will allow us to consistently incorporate radiative feedback from a central source and to test the above hypothesis.

4.2. Magnetic Fields

The ART code does not include magnetic fields, whereas MHD is certainly important for accretion disk physics (see Balbus & Hawley 1998, and references therein). It is for this reason that the present study has been restricted to scales larger than ≈ 0.1 pc, corresponding to about 10^4 Schwarzschild radii for a black hole of mass $3 \times 10^7 M_\odot$.

At scales larger than the accretion disk, the absence of magnetic fields in the ART code is probably not important. An estimate of the strength that an equipartition magnetic field would need in order to affect the disk on small scales is given by $B_{\text{eq}}^2 \approx 4\pi\rho\sigma_{\text{turb}}^2$. In order to affect the large-scale dynamics of the gas, the magnetic field would have to have an even larger strength of order $B_{\text{dyn}}^2 \approx 4\pi\rho v_t^2$. Figure 14 shows estimates of B_{eq} and B_{dyn} , in order to demonstrate how high the magnetic field would need to be to significantly influence gas dynamics in the simulated galaxy. For most of the galactic disk, the above estimates for the magnetic field are far higher than the few μ G fields observed in real galaxies (e.g. Zweibel & Heiles 1997; Beck 2001). Even in the sub-pc region, where water maser observations indicate stronger fields of a few tens of mG (e.g. Modjaz et al. 2005; Vlemmings et al. 2007), the magnetic field is still too low to affect the gas dynamics in the model galaxy. We therefore conclude that magnetic fields, which are not included in our simulations, will have a negligible effect on the dynamical state of this disk unless their strength greatly exceeds observational measurements.

5. DISCUSSION AND CONCLUSIONS

We have used a large-dynamic range cosmological simulation to study gas dynamics in the circumnuclear disk of typical mass galaxy at $z \approx 4$ (evolving into an L_* galaxy at $z = 0$), resolving the distribution of matter from megaparsec scales all the way down to sub-pc scales (with 20 levels of refinement). The simulation reveals a cold, fully molecular, self-gravitating, and turbulent

⁹ Notice, that the outer, optically thin layers of such a disk would continue cooling efficiently, covering the hot interior with a cold molecular “skin”. Such a skin may become Rayleigh-Taylor unstable, leading to fragmentation of the torus into individual clouds.

rotationally-supported gas disk, which is globally unstable but locally stable.

The global instability, operating on a range of scales comparable to the size of the system, generates turbulence down to the smallest scale resolved in the simulation. On small scales, the turbulence supports most of the disk against gravitational fragmentation and collapse. The disk, therefore, remains locally stable and reaches a quasi-stationary state. In that state, global instability drives bar-like and spiral-wave-like structures on time scales of the order of 100,000 years at 100 pc scales (and on proportionally shorter time scales at smaller radii), but on a 500,000 year time-scale the structure of the disk remains quasi-steady.

The disk develops a power-law gas density profile with a well defined slope of $-5/3$ in surface density and $-8/3$ in spherically-averaged volume density. This slope is a natural consequence of the dynamical state of the disk: the turbulence, generated by the global instability, redistributes the angular momentum in the disk on a dynamical time scale, reducing the gradient of the viscous torque. The resulting (quasi-)steady state uniquely determines the gas density profile we find in the simulation and the distribution of the angular momentum with gas mass.

The turbulence in the disk drives the local outward transport of angular momentum and the inward flow of gas toward the supermassive black hole on time scales of at least 10 million years, which are too long to follow in a single zoom-in episode of the simulation. Thus, we only capture a single snapshot in the cosmological life of the supermassive black hole. In follow-up work, we plan to consider several snapshots taken at different cosmological times in order to describe the system on longer time scales.

The dynamical state of the disk that we find in our simulation appears to be consistent with the results of previous simulations of isolated circumnuclear disks in galaxies (Fukuda et al. 2000; Wada 2001; Wada & Norman 2001; Escala 2007). A distinctive feature of our approach is that we follow the dynamics of the circumnuclear disk within cosmological simulations. While most of the volume of the simulation evolves little on time scales relevant for the dynamics of the circumnuclear disk, cosmological scales provide realistic boundary conditions for the dynamics on sub-kpc scales. Since we find that the circumnuclear disk rapidly reaches a quasi-stationary state, its evolution is entirely governed by the boundary conditions. For the same reason, the fact that the cosmological simulation that was used for the initial conditions did not resolve the scale of the circumnuclear disk, does not compromise our results: the quasi-stationary state of the disk does not depend on the initial conditions, and so the lack of power on scales below about 100 pc in the initial cosmological simulation is not important.

REFERENCES

- Abel, T., Bryan, G. L., & Norman, M. L. 2002, *Science*, 295, 93
 Balbus, S. A., & Hawley, J. F. 1998, *Reviews of Modern Physics*, 70, 1
 Beck, R. 2001, *Space Science Reviews*, 99, 243
 Bottema, R. 2003, *MNRAS*, 344, 358
 Christodoulou, D. M., Shlosman, I., & Tohline, J. E. 1995a, *ApJ*, 443, 551
 —. 1995b, *ApJ*, 443, 563

The adopted approach of this work is comparable to the recent study by Mayer et al. (2007), who used a cosmological simulation to model the coalescence of two supermassive black holes. While the detailed treatment of gas physics and the scientific questions answered by the two studies are different, many of our results are consistent with those of Mayer et al. (2007). For example, they find a similar slope for the spherically averaged density profile, although they do not elaborate on the physical mechanisms for the formation of this profile.

The local stability of the disk, supported by highly supersonic turbulence, implies that the disk is capable of continuously feeding a central black hole, uninterrupted by catastrophic bursts of star formation, which could have consumed the available fuel were the disk locally unstable. This interesting dynamical state of the disk provides a potential solution to the problem of how AGN fueling is maintained by self-gravitating gas disks (for a related discussion, see e.g. Shlosman & Begelman 1989; Rice et al. 2005; Nayakshin & King 2007).

The circumnuclear disk in the simulation extends all the way to the maximally resolved scale of ≈ 0.1 pc, which corresponds to the outer part of the black hole accretion disk. We find no toroidal-like structures on several parsec scales, which are commonly inferred to exist around AGN. A possible reason that the disk does not form an AGN torus on the appropriate scales (if it indeed, should) is the limitation imposed by our implementation of gas cooling in the code. The ART code, like all existing cosmological codes, assumes that the cooling radiation from cosmic gas escapes freely into the IGM. This assumption breaks down at the densities and temperatures reached by the simulation in the inner 10 pc. At this scale the disk becomes optically thick to its own cooling radiation from dust and molecular hydrogen. In that regime the disk may heat up and acquire a substantial amount of pressure support, which may result in a puffier, more toroidal-like configuration for the inner several parsecs of the disk. A consistent treatment of a putative AGN torus will require simulations that incorporate optically-thick cooling.

The authors thank Oleg Gnedin for his analysis of the mass profiles from the simulations. The authors also thank Mitch Begelman, Moshe Elitzur, Lucio Mayer, Brant Robertson, Isaac Shlosman, Volker Springel, Marta Volonteri, & Keiichi Wada for comments on the paper. This work was supported in part by the DOE and the NASA grant NAG 5-10842 at Fermilab and by the NSF grants AST-0134373 and AST-0507596. Supercomputer simulations were run on the IBM P690 array at the National Center for Supercomputing Applications and San Diego Supercomputing Center (under grant AST-020018N).

- Di Matteo, T., Colberg, J., Springel, V., Hernquist, L., & Sijacki, D. 2007, ArXiv e-prints, 705
 Di Matteo, T., Springel, V., & Hernquist, L. 2005, *Nature*, 433, 604
 Draine, B. T., & Lee, H. M. 1984, *ApJ*, 285, 89
 Efstatithou, G., Lake, G., & Negroponte, J. 1982, *MNRAS*, 199, 1069
 Elitzur, M., & Shlosman, I. 2006, *ApJ*, 648, L101
 Escala, A. 2007, ArXiv e-prints, 705

- Fan, X., Strauss, M. A., Schneider, D. P., Becker, R. H., White, R. L., Haiman, Z., Gregg, M., Pentericci, L., Grebel, E. K., Narayanan, V. K., Loh, Y.-S., Richards, G. T., Gunn, J. E., Lupton, R. H., Knapp, G. R., Ivezić, Ž., Brandt, W. N., Collinge, M., Hao, L., Harbeck, D., Prada, F., Schaye, J., Strateva, I., Zakamska, N., Anderson, S., Brinkmann, J., Bahcall, N. A., Lamb, D. Q., Okamura, S., Szalay, A., & York, D. G. 2003, AJ, 125, 1649
- Ferland, G. J., Korista, K. T., Verner, D. A., Ferguson, J. W., Kingdon, J. B., & Verner, E. M. 1998, PASP, 110, 761
- Ferrarese, L., & Merritt, D. 2000, ApJ, 539, L9
- Fukuda, H., Habe, A., & Wada, K. 2000, ApJ, 529, 109
- Gebhardt, K., Bender, R., Bower, G., Dressler, A., Faber, S. M., Filippenko, A. V., Green, R., Grillmair, C., Ho, L. C., Kormendy, J., Lauer, T. R., Magorrian, J., Pinkney, J., Richstone, D., & Tremaine, S. 2000, ApJ, 539, L13
- Gnedin, O. Y., Kravtsov, A. V., Klypin, A. A., & Nagai, D. 2004, ApJ, 616, 16
- Goldreich, P., & Lynden-Bell, D. 1965, MNRAS, 130, 97
- Kauffmann, G., & Haehnelt, M. 2000, MNRAS, 311, 576
- Kennicutt, Jr., R. C. 1998, ApJ, 498, 541
- Klypin, A., Kravtsov, A. V., Bullock, J. S., & Primack, J. R. 2001, ApJ, 554, 903
- Konigl, A., & Kartje, J. F. 1994, ApJ, 434, 446
- Kormendy, J., & Kennicutt, Jr., R. C. 2004, ARA&A, 42, 603
- Kravtsov, A. V. 1999, PhD thesis, AA(NEW MEXICO STATE UNIVERSITY)
- . 2003, ApJ, 590, L1
- Kravtsov, A. V., Klypin, A., & Hoffman, Y. 2002, ApJ, 571, 563
- Kravtsov, A. V., Klypin, A. A., & Khokhlov, A. M. 1997, ApJS, 111, 73
- Kritsuk, A. G., Norman, M. L., Padoan, P., & Wagner, R. 2007, ApJ, 665, 416
- Li, Y., Hernquist, L., Robertson, B., Cox, T. J., Hopkins, P. F., Springel, V., Gao, L., Di Matteo, T., Zentner, A. R., Jenkins, A., & Yoshida, N. 2007, ApJ, 665, 187
- Mac Low, M.-M., & Klessen, R. S. 2004, Reviews of Modern Physics, 76, 125
- Machacek, M. E., Bryan, G. L., & Abel, T. 2001, ApJ, 548, 509
- Magorrian, J., Tremaine, S., Richstone, D., Bender, R., Bower, G., Dressler, A., Faber, S. M., Gebhardt, K., Green, R., Grillmair, C., Kormendy, J., & Lauer, T. 1998, AJ, 115, 2285
- Malbon, R. K., Baugh, C. M., Frenk, C. S., & Lacey, C. G. 2006, ArXiv Astrophysics e-prints
- Mayer, L., Kazantzidis, S., Madau, P., Colpi, M., Quinn, T., & Wadsley, J. 2007, Science, 316, 1874
- McKee, C. F., & Ostriker, E. C. 2007, ARA&A, 45, 565
- Modjaz, M., Moran, J. M., Greenhill, L. J., & Kondratko, P. T. 2005, in Astronomical Society of the Pacific Conference Series, Vol. 340, Future Directions in High Resolution Astronomy, ed. J. Romney & M. Reid, 192–+
- Navarro, J. F., Frenk, C. S., & White, S. D. M. 1997, ApJ, 490, 493
- Nayakshin, S., & King, A. 2007, ArXiv e-prints, 705
- Noguchi, M. 1988, A&A, 203, 259
- Ossenkopf, V., & Henning, T. 1994, A&A, 291, 943
- Ostriker, J. P., & Peebles, P. J. E. 1973, ApJ, 186, 467
- Passot, T., & Vázquez-Semadeni, E. 1998, Phys. Rev. E, 58, 4501
- Polyachenko, V. L., Polyachenko, E. V., & Strel'Nikov, A. V. 1997, Astronomy Letters, 23, 483
- Pringle, J. E. 1981, ARA&A, 19, 137
- Regan, M. W., & Teuben, P. J. 2004, ApJ, 600, 595
- Rice, W. K. M., Lodato, G., & Armitage, P. J. 2005, MNRAS, 364, L56
- Ripamonti, E., & Abel, T. 2004, MNRAS, 348, 1019
- Roberts, Jr., W. W., Huntley, J. M., & van Albada, G. D. 1979, ApJ, 233, 67
- Shlosman, I., & Begelman, M. C. 1989, ApJ, 341, 685
- Shlosman, I., Begelman, M. C., & Frank, J. 1990, Nature, 345, 679
- Shlosman, I., Frank, J., & Begelman, M. C. 1989, Nature, 338, 45
- Sijacki, D., Springel, V., Di Matteo, T., & Hernquist, L. 2007, MNRAS, 380, 877
- Simkin, S. M., Su, H. J., & Schwarz, M. P. 1980, ApJ, 237, 404
- Springel, V., Di Matteo, T., & Hernquist, L. 2005, MNRAS, 361, 776
- Toomre, A. 1964, ApJ, 139, 1217
- Tremaine, S., Gebhardt, K., Bender, R., Bower, G., Dressler, A., Faber, S. M., Filippenko, A. V., Green, R., Grillmair, C., Ho, L. C., Kormendy, J., Lauer, T. R., Magorrian, J., Pinkney, J., & Richstone, D. 2002, ApJ, 574, 740
- Truelove, J. K., Klein, R. I., McKee, C. F., Holliman, II, J. H., Howell, L. H., & Greenough, J. A. 1997, ApJ, 489, L179+
- Vazquez-Semadeni, E. 1994, ApJ, 423, 681
- Vlemmings, W. H. T., Bignall, H. E., & Diamond, P. J. 2007, ApJ, 656, 198
- Volonteri, M., & Rees, M. J. 2005, ApJ, 633, 624
- . 2006, ApJ, 650, 669
- Wada, K. 2001, ApJ, 559, L41
- Wada, K., & Norman, C. A. 2001, ApJ, 547, 172
- . 2007, ApJ, 660, 276
- Wong, T., & Blitz, L. 2002, ApJ, 569, 157
- Wyse, R. F. G. 2004, ApJ, 612, L17
- Yoo, J., & Miralda-Escudé, J. 2004, ApJ, 614, L25
- Young, J. S., Allen, L., Kenney, J. D. P., Lesser, A., & Rownd, B. 1996, AJ, 112, 1903
- Zweibel, E. G., & Heiles, C. 1997, Nature, 385, 131

APPENDIX

MEASURING THE VISCOSITY

Here we address the validity of our estimate of the turbulent kinematic velocity parameter ν , which motivates the interpretation that turbulent transport of angular momentum maintains local stability and the quasi-steady state of the circumnuclear disk. Instead of a direct measurement of the viscosity, we have assumed that the viscosity depends on characteristic velocity and length scales, given by σ_{turb} and $\lambda_{\text{fast,r}}$, respectively. The accuracy of this estimate can be tested by measuring the transport of gas due to turbulent motions.

The ART code does not follow individual parcels of gas across cell boundaries, but rather advected quantities describing the gas. Therefore, in order to follow the turbulent motions of the gas, we introduce a passive scalar into the simulation which has a value of unity inside a spherical region centered on the black hole particle, and a value of zero outside this region, effectively “painting” the gas. As the simulation evolves, turbulent motions of the gas cause the profile of the scalar quantity to deviate from its original spherical form. The evolution of the profile depends on the turbulent kinematic viscosity, ν , and in the early stages of diffusion, while the deviations from the initial profile are small, the profile approximately satisfies the linear diffusion equation for initial conditions,

$$P(r, t=0) = \begin{cases} 1, & \text{if } r < r_0, \\ 0, & \text{if } r > r_0, \end{cases} \quad (\text{A1})$$

(where r_0 is the radius of the initial sphere) allowing a more direct calculation of the viscosity. The solution to the linear diffusion equation for the above initial conditions, is

$$P(x, q) = \frac{1}{2} \left[\operatorname{erf} \left(\frac{x+1}{\sqrt{q}} \right) - \operatorname{erf} \left(\frac{x-1}{\sqrt{q}} \right) \right] - \frac{q}{x\sqrt{\pi q}} e^{-(1+x^2)/q} \sinh \left(\frac{2x}{q} \right), \quad (\text{A2})$$

where

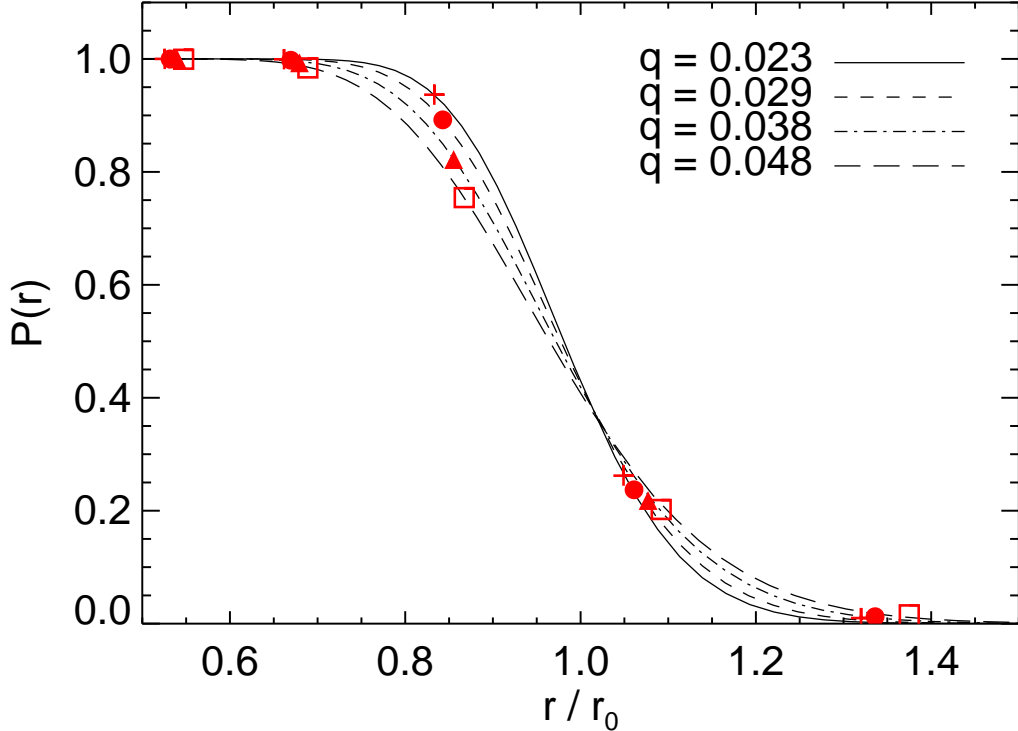


FIG. 15.— Mass-weighted profiles of the passive scalar as a function of radius, and evolving over time from a 30 pc sphere. The symbols are measurements from the simulation, and the lines are the best fits to Equation A2.

$$x = \frac{r}{r_0} \quad \& \quad q = \frac{4\nu t}{r_0^2}. \quad (\text{A3})$$

Figure 15 shows samples of the profile evolving from a 30 pc sphere for different times (q). The measured profiles agree well with the solution given in Equation A2. Starting from several painted regions at 1, 3, 10, 30, and 100 pc radii, we followed the evolution of the paint-weighted density profiles and measured the turbulent viscosity, ν , as a function of radius. Figure 16 shows the best-fit measurements of ν/r in relation to the estimate given by $\sigma_{\text{turb}}\lambda_{\text{fast},r}/r$. The lines in Figure 16 show individual snapshots of $\sigma_{\text{turb}}\lambda_{\text{fast},r}/r$ corresponding to the timescale over which the diffusion was followed (whereas Figure 9 showed a time-averaged estimate). The best-fit measurements match the estimates for ν/r well, thus lending justification to the estimate for ν used in the analytic arguments of Section 3.3.

ANGULAR MOMENTUM CONSERVATION

Anomalous numerical transport of angular momentum is sometimes presented as a concern for adaptive mesh refinement simulations using interpolation schemes for calculating velocities on the mesh. We have tested conservation of angular momentum in the code by conducting a separate set of simulations of the collapse of an isothermal sphere (the details are included in the PhD thesis of the author Levine). The test was conducted for a mesh which refined along with the collapsing sphere, and for a pre-refined mesh, in order to test the conservation of angular momentum both as the mesh refines and as gas moves through the mesh. The sphere collapses into a thin disk ($h/r \ll 1$), which conserves angular momentum over several rotation periods.

In Figure 17 we demonstrate the conservation of angular momentum in the present simulation. As the maximum resolution of the simulation increases, the angular momentum profile initially evolves, as the viscous torque, G , described in Section 3.2 redistributes angular momentum within the disk. But after reaching the maximum, level 20 resolution (the point at which we introduce the black hole particle into the simulation and let it evolve), the profile remains rather steady with time, because the disk has reached a quasi-stationary state. Figure 17 shows the angular momentum as a function of enclosed gas mass at several different times during a single zoom-in episode of the simulation. The figure shows the evolution of the angular momentum distribution from 200,000 years before the introduction of the black hole particle, when the simulation has refined to level 11, to 500,000 years after the introduction of the black hole particle, when the simulation is fully refined, and has evolved for several hundred thousand years in a quasi-steady state.

On the scale of the circumnuclear disk, the simulation has made several thousand time steps between $t = 100$ kyrs and $t = 500$ kyrs, meaning that the simulation has undergone significant evolution on this spatial scale. Numerical

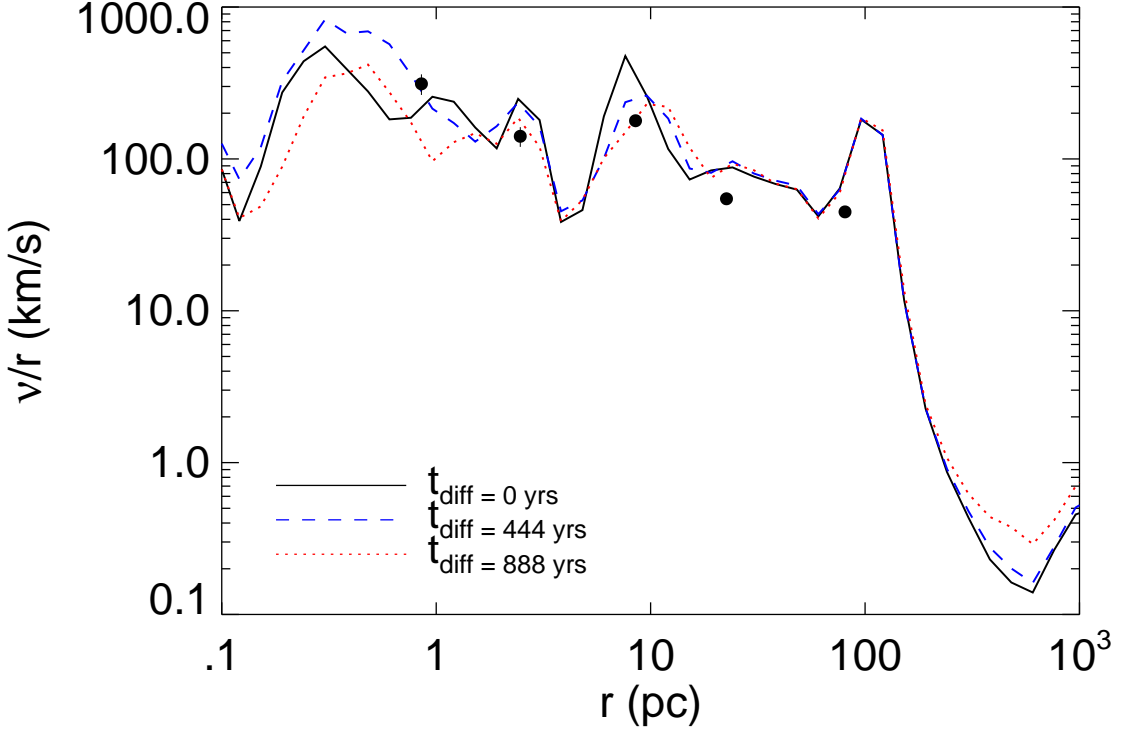


FIG. 16.— Ratio of kinematic viscosity ν , to radius R . The lines show estimates for ν/R given approximately by $\lambda_{\text{fast},r}\sigma_{\text{turb}}$, for three different snapshots. The points are estimates from a second method measuring the advection of gas at five different radii in the simulation. The snapshots correspond to the profile fits at different times, so the 1 pc point should be compared to the solid line, the next point to the dashed line, and the last three to the dotted line.

effects, accumulating with each time step, would cause deviations in the angular momentum profile. Over longer time scales, the slow inward transport of matter will alter the angular momentum profile. However, on the hundred thousand year time scale we expect the profile to remain rather steady, reflecting the quasi-stationary state of the disk, unless there is anomalous numerical transport of angular momentum. Figure 17 shows no systematic deviations in the angular momentum profile after the initial refinement and the corresponding re-distribution of the angular momentum, demonstrating that there is no sign of unphysical numerical angular momentum transport on the time scales of the simulation. On time scales much longer than those simulated in the present paper, however, these effects may become important.

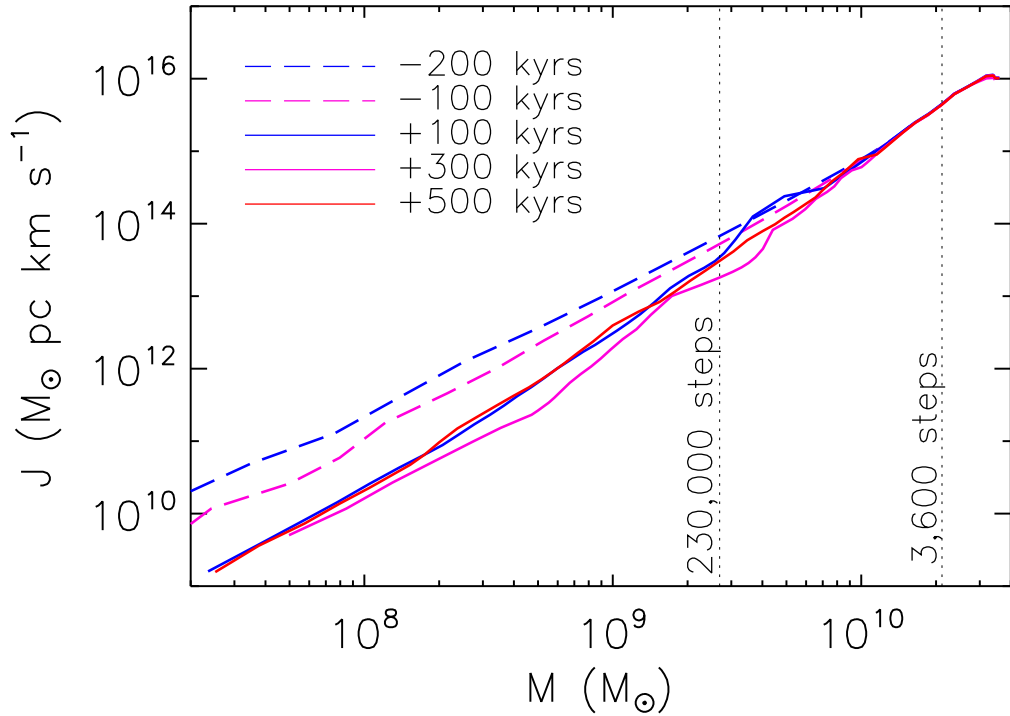


FIG. 17.— Angular momentum as a function of enclosed gas mass for several different times. The times are measured from the introduction of the black hole. The vertical dashed lines correspond to enclosed masses on scales of ≈ 10 and ≈ 1000 pc. At each of these scales, the simulation has made approximately 230,000 and 3,600 steps, respectively (corresponding to the resolution at each scale), between $t = 100$ and $t = 500$ kyrs.